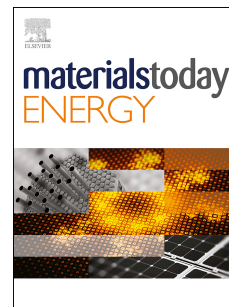


# Journal Pre-proof

2D argyrodite LPSCI solid electrolyte for all-solid-state Li ion battery using reduced graphene oxide template

Seok Hun Kang, Ju Young Kim, Dong Ok Shin, Myeong Ju Lee, Young-Gi Lee



PII: S2468-6069(21)00278-1

DOI: <https://doi.org/10.1016/j.mtener.2021.100913>

Reference: MTENER 100913

To appear in: *Materials Today Energy*

Received Date: 16 September 2021

Revised Date: 23 November 2021

Accepted Date: 23 November 2021

Please cite this article as: S.H. Kang, J.Y. Kim, D.O. Shin, M.J. Lee, Y.-G. Lee, 2D argyrodite LPSCI solid electrolyte for all-solid-state Li ion battery using reduced graphene oxide template, *Materials Today Energy*, <https://doi.org/10.1016/j.mtener.2021.100913>.

This is a PDF file of an article that has undergone enhancements after acceptance, such as the addition of a cover page and metadata, and formatting for readability, but it is not yet the definitive version of record. This version will undergo additional copyediting, typesetting and review before it is published in its final form, but we are providing this version to give early visibility of the article. Please note that, during the production process, errors may be discovered which could affect the content, and all legal disclaimers that apply to the journal pertain.

© 2021 Published by Elsevier Ltd.

## CRedit author statement

**Seok Hun Kang:** Conceptualization, Validation, Investigation, Writing - Original Draft.

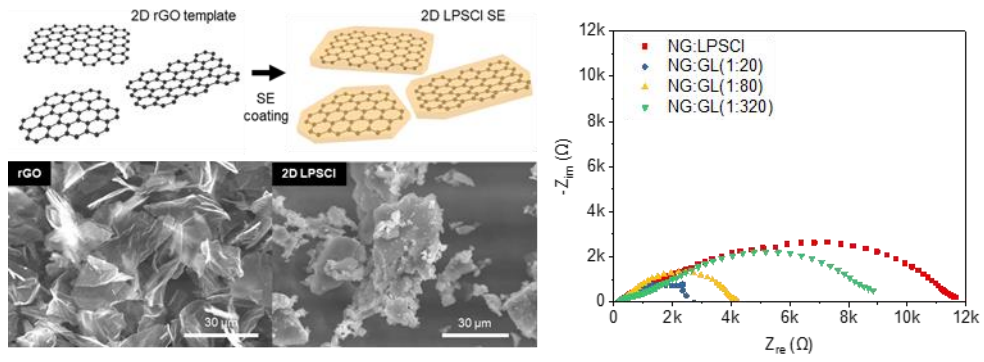
**Ju Young Kim:** Conceptualization, Methodology, Writing - Review & Editing.

**Dong Ok Shin:** Formal analysis, Resources.

**Myeong Ju Lee:** Formal analysis, Resources.

**Young-Gi Lee:** Supervision, Project administration, Funding acquisition.

Journal Pre-proof



**2D argyrodite LPSCl solid electrolyte for all-solid-state Li ion battery using reduced graphene oxide template**

Seok Hun Kang<sup>#,\*</sup>, Ju Young Kim<sup>#</sup>, Dong Ok Shin, Myeong Ju Lee, and Young-Gi Lee<sup>\*</sup>

*Reality Devices Research Division, Electronics and Telecommunications Research Institute (ETRI), 218 Gajeongno, Yuseong-gu, Daejeon 34129, Republic of Korea*

<sup>#</sup>These authors contributed equally to this work.

Corresponding authors

\*E-mail: shkang@etri.re.kr (S. H. Kang)

\*E-mail: lyg@etri.re.kr (Dr. Y-G. Lee)

Keywords: All-solid-state battery, lithium-ion battery, solid electrolyte, morphology control, argyrodite

**Abstract**

All-solid-state lithium-ion batteries (ASLBs) are regarded as the next generation of energy storage devices owing to their excellent safety. However, the performance of ASLBs has yet to reach that of currently commercialized liquid electrolyte-based lithium-ion batteries due to numerous problems including the inferior ionic conductivities of solid electrolytes (SEs) and poor solid-solid interfacial contact between the SE and active material particles. Herein, dimensional control of SE particles using liquid phase synthesis is demonstrated and its favorable impact on cell performance is investigated. Argyrodite  $\text{Li}_6\text{PS}_5\text{Cl}$  SE with high ionic conductivity of  $1.54 \text{ mS cm}^{-1}$  and distinct 2D morphology was synthesized using 2D structured reduced graphene oxide as the template. The SE particles with high aspect ratio improves the long-range connectivity of the SE within the composite electrode and provides a well-connected ionic transport pathway for charge-discharge. The electrochemical impedance spectroscopy analysis of the composite electrode using electron blocking cell configuration revealed threefold enhancement of the effective ionic transport within the composite. As a result, superior rate performance was demonstrated with 2D SE composite electrodes at high C rates.

## Introduction

Lithium-ion batteries (LIB) are essential energy storage devices that have enabled the development of the portable electronics and electric vehicles used today. The global LIB market has grown over 80 times in volume in the past two decades as LIBs have been adopted in large scale applications such as grid level stationary energy storage systems (ESS) [1-3]. However, large scale applications of LIBs have raised serious safety concerns, which are inevitable with the current battery system that utilizes flammable liquid electrolytes. Severe fires and explosions have been reported worldwide in all kinds of devices utilizing LIBs, including mobile devices, electric vehicles, and ESS [4-9].

An approach to fundamentally solve the fire and explosion hazard problems of current LIBs is to replace flammable liquid electrolytes (LEs) with intrinsically nonflammable solid electrolytes (SEs). Much research has been conducted in developing novel materials that can be utilized as SEs for all-solid-state LIBs (ASLBs) [10-19]. Among candidate materials, sulfide based SEs, especially Li-argyrodites, have received great attention due to their high ionic conductivities, which rival those of LEs, and their mechanically compliant properties, which enable more intimate contact at the active material-SE interface [20-22]. However, even with sulfide SE with high ionic conductivity of  $>10^{-3}$  S cm<sup>-1</sup>, the performance of ASLBs has yet to reach that of conventional LE-based LIBs due to limited surface coverage of active material and the restrained conduction network that results from spatial confinement of SE particles within the composite electrode. Unlike LE-based LIBs, in which the electrolyte can easily wet the active materials and ensure full contact between the active material and the electrolyte to establish an ionic conducting network within the composite electrode, proper physical contact is challenging in ASLBs due to the solid-solid contact between the active material and the electrolyte; therefore, ionic connectivity must be taken into special consideration with ASLBs

[23,24].

To address this issue, using percolation theory to establish ionic connectivity within the composite electrode of ASLBs has been studied [25]. Percolation theory describes the formation of long-range connectivity within random systems. The percolation threshold, below which macroscopic continuous phase does not exist, depends on the geometrical shape of the dispersed particles [26]. It has been shown with mathematical calculations that the percolation threshold varies inversely with the particle's aspect ratio and thus long-range connectivity can be more easily realized with particles with higher structural anisotropy. This theory was directly implemented on the ASLB electrode system by Park and Kim et al. using computational simulation. Park compared the percolation thresholds of 0-dimensional (0D), 1-dimensional (1D), and 2-dimensional (2D) solid oxide electrolytes in 3-dimensional (3D) virtual space and showed that lower volume fraction of SE is needed with 1D and 2D SE than with 0D SE to form the shortest percolation pathway. In their ASLB, Lu et al. also demonstrated a 3D interconnected structure made of 1D  $\text{Li}_7\text{La}_3\text{Zr}_2\text{O}_{12}$  nanofibers to provide long-range transfer pathways for Li ions [27].

In this work, we take the concept further and realize a 2D structured sulfide SE using reduced graphene oxide (rGO) as the template and implement it in the composite electrode to create a high performance ASLB. Using a scalable and cost-effective liquid phase process, 2D structured argyrodite  $\text{Li}_6\text{PS}_5\text{Cl}$  (LPSCl) SE with high ionic conductivity of  $1.54 \text{ mS cm}^{-1}$  was fabricated using acetonitrile (ACN) as the solvent and rGO as the template. The as-formed 2D LPSCl exhibits mixed electrical and ionic conductance owing to the electrically conductive rGO template. 2D LPSCl was utilized with natural graphite (NG) to form composite electrodes with enhanced performance that results from improved ionic transport within the composite due to the 2D structured SE with high aspect ratio.

## Results and Discussion

The fabrication process of 2D LPSCl is schematically illustrated in Figure 1a. Stoichiometric amounts of  $\text{Li}_2\text{S}$ ,  $\text{P}_2\text{S}_5$ , and  $\text{LiCl}$  were used as the precursors, ACN was used as the solvent for liquid phase process, and rGO was used as the template for 2D morphology. Various weight ratios of rGO to LPSCl precursors were prepared and, from here on, samples will be denoted as GL1:x, in which 1:x is the weight ratio of rGO:LPSCl. Liquid phase fabrication has the advantages of high scalability and low fabrication cost, and allows uniform coating of SE on the rGO template. Among several solvent candidates reported in literature, ACN was chosen due to its high compatibility with sulfide SEs [28-31]. After mixing all the components, the mixed suspension was completely dried and sintered at  $550\text{ }^\circ\text{C}$  for 5 hours to form the argyrodite phase [32-34]. 0D LPSCl, used as the reference sample, was synthesized using the same procedure as above except that rGO was not added to the suspension. The size of the SE particles was adjusted to below  $20\text{ }\mu\text{m}$ , using a sieving procedure to minimize the effect of particle size and to focus on the effect of the particle structure.

Fig. 1b shows scanning electron microscope (SEM) images of the rGO template and the synthesized 2D LPSCl. The 2D flake-like morphology is distinct in both images, indicating successful morphology control of LPSCl using rGO template based synthesis. In contrast, the SEM images of a single 0D LPSCl particle shown at various tilted angles (Fig. S1) reveal round 0D morphology. For comparison, SEM images of the 2D LPSCl particle in Fig. 1b at various tilted angles are also presented in Fig. 1c. A rough approximation of the aspect ratio of GL(1:80), as observed in the SEM images, is 4.84:1. The energy dispersive X-ray spectroscopy (EDS) mapping images of the 2D LPSCl in Fig. S2 show uniform dispersion of P, S, and Cl elements on rGO, represented by C element signals, indicating conformal coating of LPSCl on the rGO template.

The amount of rGO used to synthesize the 2D LPSCl was varied for optimal performance. Various weight ratios of rGO to LPSCl precursors were prepared and analyzed with SEM and EDS as shown in Fig. S3. All images indicate uniform coating of LPSCl on the rGO surface. Close inspection of the SEM images reveals that as the weight ratio of rGO to LPSCl precursors decreases, the particle morphology becomes closer to 0D. At a weight ratio of 1:320, the amount of LPSCl is excessively high compared to the amount of rGO and small LPSCl particles that do not adhere to the rGO surface can be seen in the EDS images.

The ionic conductivity of the 0D LPSCl was measured using electrochemical impedance spectroscopy (EIS), as shown in Fig. 2a. LPSCl synthesized in liquid phase using ACN solvent exhibits high ionic conductivity of  $1.54 \text{ mS cm}^{-1}$  at room temperature, comparable to that of mechanochemically synthesized LPSCl reported in literature [33,35]. The liquid phase technique shows great benefits in terms of commercialization due to its high scalability and yield. Using the proposed liquid phase technique, a large batch of 50 g LPSCl with high ionic conductivity on the order of  $10^{-3} \text{ S cm}^{-1}$  was synthesized in a single batch with yield as high as 96%, using cheap lab-scale equipment (Fig. S4).

Interestingly, because of the use of electrically conductive rGO, the 2D LPSCl exhibited mixed ionic and electronic conductance. rGO, used as template for 2D LPSCl, was thermally reduced at high temperature and, as a result, a large amount of oxygen functional groups were removed and some of the graphitic lattice was restored [36]. The Nyquist plot of GL(1:20), shown in Fig. S5, displays distinctively different behavior compared to that of the 0D LPSCl. The best-fitting result of the experimental Nyquist plot using the equivalent circuit, in the inset of Fig. S5, reveals ionic conductivity of  $0.85 \text{ mS cm}^{-1}$  and electronic conductivity of  $5.47 \text{ mS cm}^{-1}$ . When rGO is used in excess, electrically conductive rGO flakes can form long-range electronic connectivity in the SE matrix and simultaneously reduce the effective ionic conductivity by hindering the flow of Li ions.

X-ray diffraction (XRD) analysis results of the synthesized LPSCI are shown in Fig. 2b. All samples show similar peaks corresponding to the argyrodite phase (space group F-43m) of LPSCI [37]. Minor traces of LiCl, Li<sub>2</sub>S, and Li<sub>3</sub>PO<sub>4</sub> impurities were seen, as previously reported in the literature, which are possibly the result of remnant precursors and residual moisture in the mixed suspension [38]. Differences in peak intensities and peak positions between 0D LPSCI and 2D LPSCI are almost negligible, which implies that the LPSCI coating layer of 2D LPSCI is the same material as 0D LPSCI and it is also clear that rGO does not induce an undesirable side reaction during LPSCI synthesis. The rGO XRD peak shown in Fig. S6 could not be detected in the 2D LPSCI XRD patterns, indicating well-dispersed rGO during the liquid phase synthesis. Although the ionic conductivities of 2D LPSCI could not be directly measured due to the mixed conductance resulting from the electrically conductive rGO, from the XRD results, we could deduce that the LPSCI coating layer of 2D LPSCI exhibits ionic conductivity similar to that of 0D LPSCI.

Unlike conventional liquid electrolyte-based LIBs, the spatial configuration of the SE and active material particles in the composite electrode must be carefully considered for high performance ASLBs. Although the ionic conductivity of SE is an intrinsic material property, the effective ionic transport within the composite electrode can differ depending on extrinsic factors such as particle size, particle morphology, distribution, etc. The effective ionic conductivities within the composite electrodes were analyzed with EIS using the electron blocking cell configuration shown in the inset of Fig. 3a. Using this configuration, Li ion transport resistance of the composite can be obtained by limiting the flow of electrons in the cell [39]. The impedance at high frequencies resembles the resistance of the SE layers:

$$Z_{\text{high f.}} = R_{\text{electrolyte}}$$

The impedance at low frequency resembles the sum of the SE layer resistance and the ionic

transport resistance within the composite layer:[39]

$$Z_{\text{low f.}} = R_{\text{electrolyte}} + R_{\text{ion}}$$

Because the thickness of the SE layer was kept constant for all cells, the initial impedances at high frequencies start at similar levels for all samples. However, at low frequencies, the EIS plots of the composites made with 2D LPSCI contrast dramatically with that of the composite made with 0D LPSCI. In general, the ionic transport resistance decreases for 2D LPSCI composites. According to percolation theory, long-range connectivity can be improved for particles with higher aspect ratio. Due to its 2D morphology, 2D LPSCI exhibits enhanced effective ionic transport within the composite despite constant intrinsic ionic conductivity. The calculated ionic transport resistances within the composites are compared in Fig. 3b. We note that the ionic transport resistance of the NG:GL(1:20) composite could not be measured with the proposed setup. This is most likely due to the extremely high tortuosity generated within the composite when rGO is used in excess. Therefore, the composition of rGO:LPSCI must be optimized to achieve the highest effective ionic transport conductivity. The effective ionic transport conductivity within the composite of the NG:GL(1:80) was  $2.9 \times 10^{-6} \text{ S cm}^{-1}$ , which is 3 times greater than that of the NG:LPSCI ( $1.0 \times 10^{-6} \text{ S cm}^{-1}$ ). The measured impedance values and calculated ionic transport resistances of all composites are listed in Table 1.

To confirm the enhanced performance of the composite electrodes using 2D SE particles, half-cell tests were performed using Li metal as the anode and LPSCI pellet as the electrolyte layer. Fig. 4a and S7 provides cross sectional images of the composite electrodes before the charge-discharge test. EDS mapping images reveal uniform distribution of LPSCI SE and NG active material particles within the composite layer. The charge-discharge profiles of each composite electrode at 0.1C rate for the first 3 cycles are shown in Fig. S8. All cells exhibit specific capacities close to the theoretical capacity of graphite ( $372 \text{ mAh g}^{-1}$ ). The

specific capacities at the third cycle were 330, 326, 322, and 311 mAh g<sup>-1</sup> for NG:LPSCl, NG:GL(1:20), NG:GL(1:80), and NG:GL(1:320), respectively. As shown in Fig. S9, all cells exhibited relatively low Coulombic efficiencies in the first cycle (below 78%), which is attributed to the decomposition of LPSCl at the active material and electrolyte interface, as previously reported in the literature [29,40]. Interestingly, although the 0D LPSCl composite showed a capacity at 0.1C rate slightly higher than that of the 2D LPSCl composites, the 2D LPSCl composites outperformed the 0D LPSCl composite at higher rates. As shown in Fig. 4b and 4c, NG:GL(1:80) and NG:GL(1:320) outperform NG:LPSCl at all rates above the 0.3C rate. The specific capacities of NG:LPSCl, NG:GL(1:80), and NG:GL(1:320) at 1C rate were 216, 241, and 228 mAh g<sup>-1</sup>, respectively. Calculating the capacity retentions at the 1C rate relative to the specific capacities at the 0.1C rate, the capacity retentions of NG:LPSCl, NG:GL(1:80), and NG:GL(1:320) were 65.3, 74.7, and 72.9%, respectively. The superior rate performance can be attributed to the improved ionic transport within the composite, resulting from the well-connected SE particles with high aspect ratio, as shown in the EIS analysis. In a similar manner, NG:GL(1:20) exhibited relatively low specific capacity of 199 mAh g<sup>-1</sup> at 1C rate, which was 61.1% of that at the 0.1C rate, due to impeded ionic transport within the composite resulting from the extremely high tortuosity generated by excess amount of rGO.

The 2D LPSCl composites also demonstrated improved cyclic stability in comparison to the 0D LPSCl composite. Careful inspection of the cycling stability at 0.3C from the 29th cycle to 78th cycle in Fig. 4b reveals enhanced cycling stabilities of NG:GL(1:80) and NG:GL(1:320) than those of NG:LPSCl and NG:GL(1:20). More specifically, calculating the capacity retention at the 78th cycle relative to the 29th cycle, the capacity retention of NG:LPSCl, NG:GL(1:20), NG:GL(1:80), NG:GL(1:320) is 83.6, 82.9, 95.3, 92.8%, respectively. The enhanced cyclic stability for NG:GL(1:80) and NG:GL(1:320) arise from the improved SE percolation and thus higher effective ionic conductivity within the composite electrode. This

indicates facile transport of Li ions to all parts of the electrode, which enables most of the active material to involve in continuous electrochemical reaction. On the other hand, composite using 0D SE particles displayed lower effective ionic conductivity within the composite which indicates limited Li ion transport in the composite electrode. The amount of active material that can actively involve in charge-discharge decreases, which led to lower cyclic performance.

To confirm that the improved rate performance resulted from the morphology control of SE particles, the capacity contribution from rGO was also investigated. As shown in Fig. S10, GL(1:80) SE was tested as active material for the charge-discharge test; it can be seen that the capacity contribution from rGO was negligible. By simply modifying the morphology of the SE particles, the entire cell performance can be improved, even with the same SE material and electrode composition.

## Conclusion

In summary, the morphology of sulfide SE particles was successfully modified using rGO template method and the impact of this modification on the overall ionic transport within the composite electrode and on the cell performance was examined. Using scalable and cost-effective liquid phase synthesis, LPSCl SE particles with 2D morphology were synthesized by conformal coating of LPSCl on rGO flakes. Due to the favorable ionic percolation that results from the high aspect ratio of SE particles, the effective ionic conductivity within the composite electrode was improved threefold and the favorable effect of this improvement on the rate performance was examined via half-cell test. Furthermore, the synthesized 2D SE showed mixed ionic and electronic conductance resulting from the electrically conductive rGO template; we expect this type of SE to show better performance when used with nonconductive active materials. The suggested morphology control is not limited to sulfide SEs, and we believe the insights provided in this paper will contribute to realizing high performance ASLBs suitable for commercialization.

## Experimental Procedure

### *Fabrication of LPSCl SE*

2D LPSCl was prepared by liquid phase process and subsequent heat treatment in argon environment. A stoichiometric mixture of  $\text{Li}_2\text{S}$  (99.9%, Alfa Aesar),  $\text{P}_2\text{S}_5$  (99%, Sigma-Aldrich), and  $\text{LiCl}$  (99.98%, Sigma-Aldrich) powders was added to ACN (anhydrous 99.8%, Sigma-Aldrich) solvent and mixed using a magnetic stirring bar for 1 h. rGO powder was subsequently added to the mixture, which was stirred for an additional 1 h. The mixed suspension was dried on a hot plate at 120 °C until solvent was completely evaporated. Remaining powder was heat treated using a muffle furnace at 550 °C for 5 h. Final sintered powder was sieved with 20  $\mu\text{m}$  sieve before use.

0D LPSCl was prepared using the same procedure as above, except rGO was not added to the suspension. rGO powder, which was used as the template, was produced by thermally reducing GO powder (GO-V50, Standard Graphene) at 1000 °C in vacuum for 10 h. rGO powder was sieved with 20  $\mu\text{m}$  sieve before use as 2D template. The entire process was performed in an argon glove box.

### *Fabrication of composite electrode*

Composite electrodes were prepared using LPSCl SE powders synthesized by the procedure mentioned above. NG (LG Chem.) powders were used as active material. NG and LPSCl SE were dry-mixed with weight ratio of 7:3 using a planetary centrifugal mixer (AR-100, Thinky Mixer) without any solvent at 2000 rpm for 10 min. The mixed powder was directly used as the composite electrode for the half-cell test and EIS analysis.

### *ASLB assembly*

150 mg of LPSCl powder (Jeong Kwan Display Corporation) was cold pressed at 6

tons using a poly(ether ether ketone)(PEEK) mold with a diameter of 13 mm. On one side of the cold pressed LPSCl pellet, 10 mg of composite electrode powder was spread and cold pressed at 1 ton. On the other side of the LPSCl pellet, Li foil (300  $\mu\text{m}$ , Honjo Metal Co.) with a diameter of 12 mm was attached. The entire cell was subjected to constant uniaxial pressure by tightening the screws of a split type pressure jig with 4 Nm torque before conducting the electrochemical measurements.

#### *Electron blocking cell assembly*

150 mg of LPSCl powder (Jeong Kwan Display Corporation) was cold pressed at 1 ton using a PEEK mold with a diameter of 13 mm. On one side of the cold pressed LPSCl pellet, 30 mg of composite electrode powder was spread and cold pressed at 1 ton. Subsequently, an additional 150 mg of LPSCl powder was cold pressed at 1 ton on top of the composite electrode layer. On both sides of the entire pellet, Li foil (300  $\mu\text{m}$ , Honjo Metal Co.) with a diameter of 12 mm was attached to make the electron blocking cell for EIS measurements.

#### *Material characterization*

Scanning electron microscopy (SEM, SEC SNE-4500M) and energy dispersive X-ray spectroscopy (EDS, Bruker XFlash 640H Mini) were utilized for structural analysis and elemental mapping, respectively. SE powders were sealed with polyimide film in an argon glovebox before conducting X-ray diffraction (XRD, Rigaku, Smartlab) measurements.

#### *Electrochemical characterization*

Ionic conductivities were measured using electrochemical impedance spectroscopy (EIS) with amplitude of 15 mV and frequency range of 10 MHz to 10 mHz. The fitting of the experimental impedance was carried out with EC-lab software (BioLogic). The 2D LPSCl samples for the conductivity measurements were prepared by cold pressing the SE powders at

6 tons. Electron blocking cell configuration was used for the ionic conductivity measurements of the composite electrodes. All charge-discharge tests were conducted in a 60 °C chamber using a cycle tester (Toyo System). Constant current/constant voltage (CC/CV) and constant current (CC) modes were used for discharge and charge, respectively. The cut-off voltage was set at 0 and 2 V and the cut-off current in the CV mode was set at one fifth of the original current.

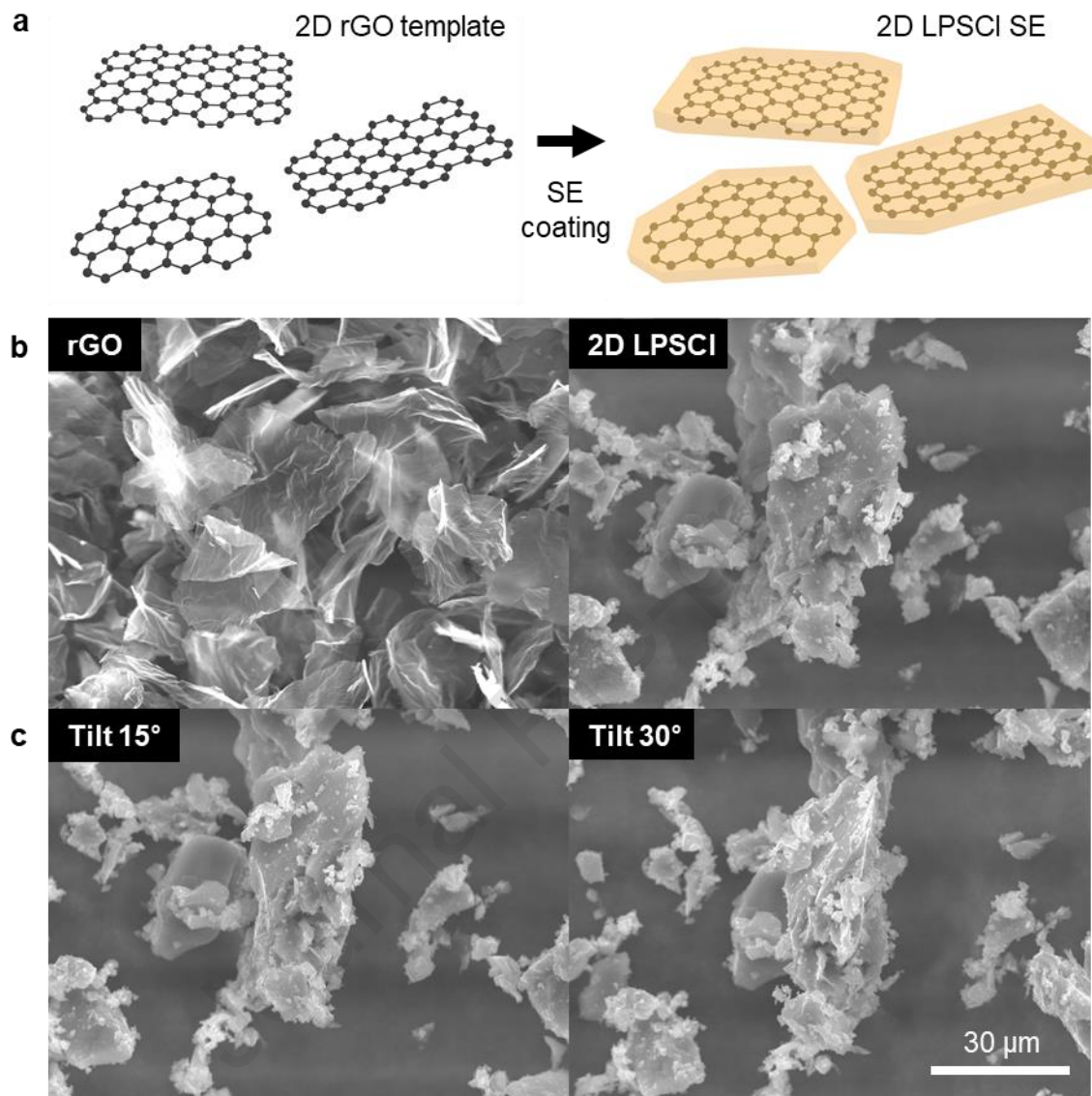


**Fig. 1.** a) Schematic illustration of 2D LPSCI SE. b) SEM images of rGO template and 2D LPSCI SE. c) Additional SEM images of 2D LPSCI in Fig. 1b) at various tilted angles.

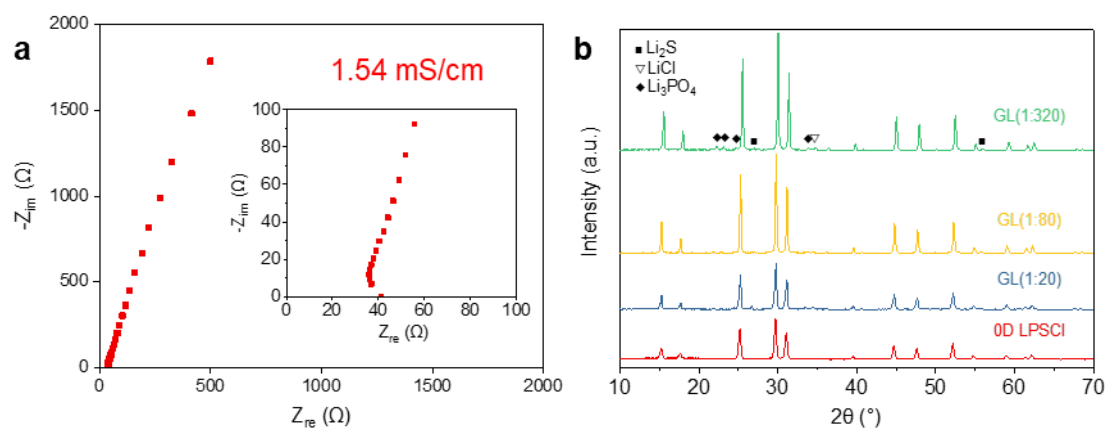


**Fig. 2.** a) Nyquist plots of 0D LPSCI and its calculated ionic conductivity. b) XRD patterns of synthesized LPSCI SEs.

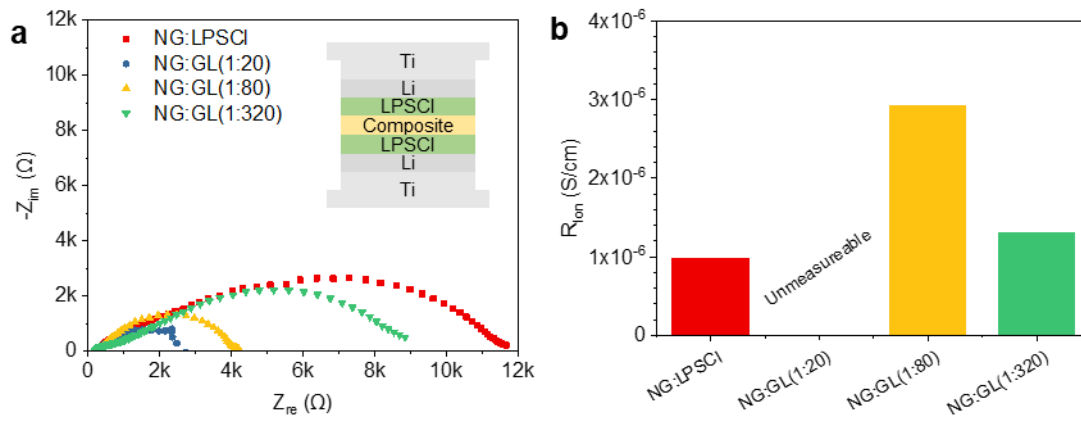


**Fig. 3.** a) Nyquist plots of composite electrodes made from various LPSCI SEs using the electron blocking cell configuration. Inset image shows schematic illustration of the electron blocking cell configuration. b) Calculated ionic conductivities within composite electrodes.

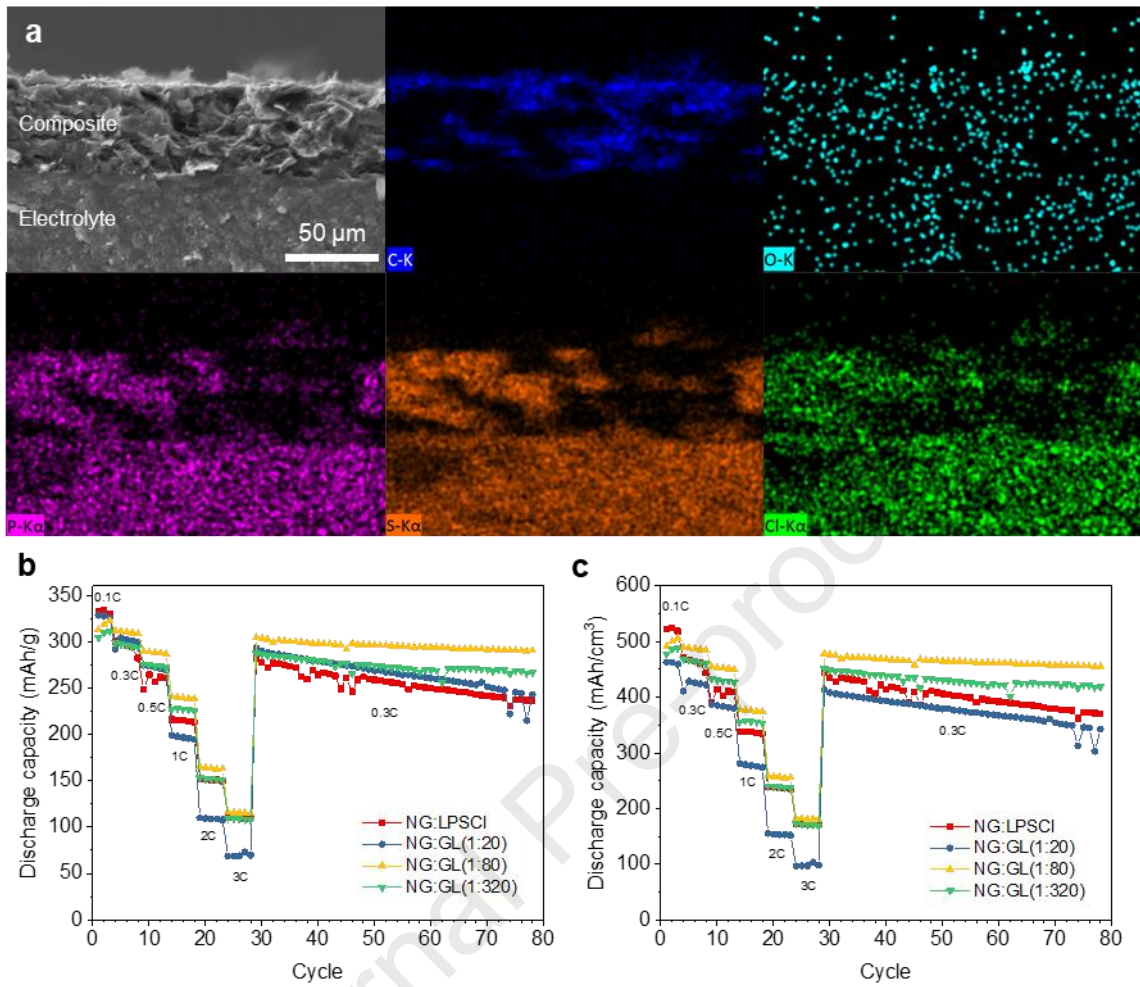


**Fig. 4.** a) Cross sectional SEM and EDS images of 2D LPSCI composite electrode. b) Gravimetric and c) volumetric rate performance and capacity retention of composite electrodes.

**Table 1**

Calculated ionic conductivities within composite electrodes.

Sample	$Z_{\text{low f.}} (\Omega)$	$Z_{\text{high f.}} (\Omega)$	$\sigma_{\text{ion}} (10^{-6} \text{ S/cm})$
NG:LPSCI	11509	262	1.0
NG:GL(1:320)	8840	197	1.3
NG:GL(1:80)	4062	188	2.9
NG:GL(1:20)	-	158	-

**Data availability**

The raw/processed data required to reproduce these findings cannot be shared at this time as the data also form part of an ongoing study.

**Acknowledgements**

This work was supported by the Electronics and Telecommunications Research Institute (ETRI) grant funded by the Korea government [20ZB1200, Development of ICT Materials, Components and Equipment Technologies], the Technology Development Program to Solve Climate Changes of the National Research Foundation (NRF) funded by the Ministry of Science & ICT (2017M1A2A2044492), and the Technology Innovation Program (20012326) funded by the Ministry of Trade, Industry & Energy(MOTIE, Korea).

S. H. Kang and J. Y. Kim contributed equally to this work.

**Supplementary data**

Supplementary data related to this article can be found at DOI.

## References

- [1] C. Pillot, The rechargeable battery market and main trends 2018-2030. In *36th Annual International Battery Seminar & Exhibit. Avicenne Energy*, (2019)
- [2] K. H. Park, Q. Bai, D. H. Kim, D. Y. Oh, Y. Zhu, Y. Mo, Y. S. Jung, Design strategies, practical considerations, and new solution processes of sulfide solid electrolytes for all-solid state batteries, *Adv. Energy Mater.* (2018) **8**, 1800035. <https://doi.org/10.1002/aenm.201800035>
- [3] K. N. Jung, H. S. Shin, M. S. Park, J. W. Lee, Solid-State Lithium Batteries: Bipolar Design, Fabrication, and Electrochemistry, *ChemElectroChem* (2019) **6**, 3842-3859. <https://doi.org/10.1002/celec.201900736>
- [4] Q. Wang, P. Ping, X. Zhao, G. Chu, J. Sun, C. Chen, Thermal runaway caused fire and explosion of lithium ion battery, *J. Power Sources* (2012) **208**, 210-224. <https://doi.org/10.1016/j.jpowsour.2012.02.038>
- [5] M. J. Loveridge, G. Remy, N. Kourra, R. Genieser, A. Barai, M. J. Lain, Y. Guo, M. Amor-Segan, M. A. Williams, T. Amietszajew, Looking deeper into the Galaxy (Note 7), *Batteries* (2018) **4**, 3. <https://doi.org/10.3390/batteries4010003>
- [6] K.-M. Park, J.-H. Kim, J.-Y. Park, S.-B. Bang, A Study on the Fire Risk of ESS through Fire Status and Field Investigation, *Fire Sci. Eng.* (2018) **32**, 91-99. <https://doi.org/10.7731/KIFSE.2018.32.6.091>
- [7] L. Kong, C. Li, J. Jiang, M. G. Pecht, Li-ion battery fire hazards and safety strategies, *Energies* (2018) **11**, 2191. <https://doi.org/10.3390/en11092191>
- [8] K. Liu, Y. Liu, D. Lin, A. Pei, Y. Cui, Materials for lithium-ion battery safety, *Sci. Adv.* (2018) **4**, eaas9820. <https://doi.org/10.1126/sciadv.aas9820>
- [9] F. Larsson, P. Andersson, B.-E. Mellander, Lithium-ion battery aspects on fires in electrified vehicles on the basis of experimental abuse tests, *Batteries* (2016) **2**, 9. <https://doi.org/10.3390/batteries2020009>
- [10] J. Lau, R. H. DeBlock, D. M. Butts, D. S. Ashby, C. S. Choi, B. S. Dunn, Sulfide solid electrolytes for lithium battery applications, *Adv. Energy Mater.* (2018) **8**, 1800933. <https://doi.org/10.1002/aenm.201800933>
- [11] L. Yang, Z. Wang, Y. Feng, R. Tan, Y. Zuo, R. Gao, Y. Zhao, L. Han, Z. Wang, F. Pan, Flexible Composite Solid Electrolyte Facilitating Highly Stable “Soft Contacting” Li-Electrolyte Interface for Solid State Lithium-Ion Batteries, *Adv. Energy Mater.* (2017) **7**, 1701437. <https://doi.org/10.1002/aenm.201701437>
- [12] A. C. Luntz, J. Voss, K. Reuter, Interfacial challenges in solid-state Li ion batteries, *J. Phys. Chem* (2015), 4899-4604. <https://doi.org/10.1021/acs.jpcclett.5b02352>
- [13] Y. S. Jung, D. Y. Oh, Y. J. Nam, K. H. Park, Issues and challenges for bulk-type all-solid-state rechargeable lithium batteries using sulfide solid electrolytes, *Isr. J. Chem.* (2015) **55**, 472-485. <https://doi.org/10.1002/ijch.201400112>
- [14] N. Kamaya, K. Homma, Y. Yamakawa, M. Hirayama, R. Kanno, M. Yonemura, T. Kamiyama, Y. Kato, S. Hama, K. Kawamoto, A lithium superionic conductor, *Nat. Mater* (2011) **10**, 682-686. <https://doi.org/10.1038/NMAT3066>
- [15] A. Hayashi, K. Noi, A. Sakuda, M. Tatsumisago, Superionic glass-ceramic electrolytes for room-temperature rechargeable sodium batteries, *Nat. Commun.* (2012) **3**, 1-5. <https://doi.org/10.1038/ncomms1843>
- [16] K. Takada, Progress and prospective of solid-state lithium batteries, *Acta Mater.* (2013) **61**, 759-770. <https://doi.org/10.1016/j.actamat.2012.10.034>
- [17] Q. Zhao, L. Zhang, B. He, A. Ye, M. Avdeev, L. Chen, S. Shi, Identifying descriptors for Li<sup>+</sup> conduction in cubic Li-argyrodites via hierarchically encoding crystal structure and

- inferring causality, *Energy Storage Mater.* (2021) **40**, 386-393. <https://doi.org/10.1016/j.ensm.2021.05.033>
- [18] Q. Zhao, M. Avdeev, L. Chen, S. Shi, Machine learning prediction of activation energy in cubic Li-argyrodites with hierarchically encoding crystal structure-based (HECS) descriptors, *Sci. Bull.* (2021) **66**, 1401-1408. <https://doi.org/10.1016/j.scib.2021.04.029>
- [19] F. Mizuno, A. Hayashi, K. Tadanaga, M. Tatsumisago, New, highly ion-conductive crystals precipitated from Li<sub>2</sub>S–P<sub>2</sub>S<sub>5</sub> glasses, *Adv. Mater.* (2005) **17**, 918-921. <https://doi.org/10.1002/adma.200401286>
- [20] H.-J. Deiseroth, S.-T. Kong, H. Eckert, J. Vannahme, C. Reiner, T. Zaiß, M. Schlosser, Li<sub>6</sub>PS<sub>5</sub>X: A Class of Crystalline Li-Rich Solids With an Unusually High Li<sup>+</sup> Mobility, *Angew. Chem. Int. Ed.* (2008) **47**, 755-758. <https://doi.org/10.1002/anie.200703900>
- [21] C. Yu, F. Zhao, J. Luo, L. Zhang, X. Sun, Recent development of lithium argyrodite solid-state electrolytes for solid-state batteries: Synthesis, structure, stability and dynamics, *Nano Energy* (2021) **83**, 105858. <https://doi.org/10.1016/j.nanoen.2021.105858>
- [22] L. Zhou, N. Minafra, W. G. Zeier, L. F. Nazar, Innovative Approaches to Li-Argyrodite Solid Electrolytes for All-Solid-State Lithium Batteries, *Acc. Chem. Res.* (2021) **54**, 2717-2728. <https://doi.org/10.1021/acs.accounts.0c00874>
- [23] J. Y. Kim, J. Kim, S. H. Kang, D. O. Shin, M. J. Lee, J. Oh, Y. G. Lee, K. M. Kim, Efficient cell design and fabrication of concentration-gradient composite electrodes for high power and high-energy-density all-solid-state batteries, *ETRI J.* (2020) **42**, 129-137. <https://doi.org/10.4218/etrij.2019-0176>
- [24] M. S. Indu, G. V. Alexander, O. V. Sreejith, S. E. Abraham, R. Murugan, Lithium garnet-cathode interfacial chemistry: inclusive insights and outlook toward practical solid-state lithium metal batteries, *Mater. Today Energy* (2021) **21**, 100804. <https://doi.org/10.1016/j.mtener.2021.100804>
- [25] J. Park, J. Y. Kim, D. O. Shin, J. Oh, J. Kim, M. J. Lee, Y.-G. Lee, M.-H. Ryou, Y. M. Lee, Dimension-controlled solid oxide electrolytes for all-solid-state electrodes: Percolation pathways, specific contact area, and effective ionic conductivity, *Chem. Eng. J.* (2019), 123528. <https://doi.org/10.1016/j.cej.2019.123528>
- [26] E. J. Garboczi, K. A. Snyder, J. F. Douglas, M. F. Thorpe, Geometrical percolation threshold of overlapping ellipsoids, *Phys. Rev. E* (1995) **52**, 819-828. <https://doi.org/10.1103/PhysRevE.52.819>
- [27] Y. Lu, X. Zhang, C. Xue, C. Xin, M. Li, C.-w. Nan, Y. Shen, Three-dimensional structured asymmetric electrolytes for high interface stability and fast Li-ion transport in solid-state Li-metal batteries, *Mater. Today Energy* (2020) **18**, 100522. <https://doi.org/10.1016/j.mtener.2020.100522>
- [28] S. Yubuchi, W. Nakamura, T. Bibienne, S. Rousselot, L. W. Taylor, M. Pasquali, M. Dollé, A. Sakuda, A. Hayashi, M. Tatsumisago, All-solid-state cells with Li<sub>4</sub>Ti<sub>5</sub>O<sub>12</sub>/carbon nanotube composite electrodes prepared by infiltration with argyrodite sulfide-based solid electrolytes via liquid-phase processing, *J. Power Sources* (2019) **417**, 125-131. <https://doi.org/10.1016/j.jpowsour.2019.01.070>
- [29] D. H. Kim, D. Y. Oh, K. H. Park, Y. E. Choi, Y. J. Nam, H. A. Lee, S.-M. Lee, Y. S. Jung, Infiltration of solution-processable solid electrolytes into conventional Li-ion-battery electrodes for all-solid-state Li-ion batteries, *Nano Lett.* (2017) **17**, 3013-3020. <https://doi.org/10.1021/acs.nanolett.7b00330>
- [30] A. Miura, N. C. Rosero-Navarro, A. Sakuda, K. Tadanaga, N. H. Phuc, A. Matsuda, N. Machida, A. Hayashi, M. Tatsumisago, Liquid-phase syntheses of sulfide electrolytes for all-solid-state lithium battery, *Nat. Rev. Chem.* (2019) **3**, 189-198. <https://doi.org/10.1038/s41570-019-0078-2>

- [31] K. Lee, S. Kim, J. Park, S. H. Park, A. Coskun, D. S. Jung, W. Cho, J. W. Choi, Selection of binder and solvent for solution-processed all-solid-state battery, *J. Electrochem. Soc.* (2017) **164**, A2075. <https://doi.org/10.1149/2.1341709jes>
- [32] C. Yu, S. Ganapathy, J. Hageman, L. van Eijck, E. R. Van Eck, L. Zhang, T. Schwietert, S. Basak, E. M. Kelder, M. Wagemaker, Facile synthesis toward the optimal structure-conductivity characteristics of the argyrodite Li<sub>6</sub>PS<sub>5</sub>Cl solid-state electrolyte, *ACS Appl. Mater. Interfaces* (2018) **10**, 33296-33306. <https://doi.org/10.1021/acsami.8b07476>
- [33] R. P. Rao, and S. Adams, Studies of lithium argyrodite solid electrolytes for all-solid-state batteries, *Phys. Status Solidi A* (2011) **208**, 1804-1807. <https://doi.org/10.1002/pssa.201001117>
- [34] Z. Zhang, L. Zhang, Y. Liu, C. Yu, X. Yan, B. Xu, L.-m. Wang, Synthesis and characterization of argyrodite solid electrolytes for all-solid-state Li-ion batteries, *J. Alloys Compd.* (2018) **747**, 227-235. <https://doi.org/10.1016/j.jallcom.2018.03.027>
- [35] S. Boulineau, M. Courty, J.-M. Tarascon, V. Viallet, Mechanochemical synthesis of Li-argyrodite Li<sub>6</sub>PS<sub>5</sub>X (X=Cl, Br, I) as sulfur-based solid electrolytes for all solid state batteries application, *Solid State Ion.* (2012) **221**, 1-5. <https://doi.org/10.1016/j.ssi.2012.06.008>
- [36] S. H. Kang, I. G. Kim, B.-N. Kim, J. H. Sul, Y. S. Kim, I.-K. You, Facile Fabrication of Flexible In-Plane Graphene Micro-Supercapacitor via Flash Reduction, *ETRI J.* (2018) **40**, 275-282. <https://doi.org/10.4218/etrij.2017-0242>
- [37] L. Zhou, K.-H. Park, X. Sun, F. Lalère, T. Adermann, P. Hartmann, L. F. Nazar, Solvent-Engineered Design of Argyrodite Li<sub>6</sub>PS<sub>5</sub>X (X = Cl, Br, I) Solid Electrolytes with High Ionic Conductivity, *ACS Energy Lett.* (2019) **4**, 265-270. <https://doi.org/10.1021/acseenergylett.8b01997>
- [38] M. A. Kraft, S. P. Culver, M. Calderon, F. Böcher, T. Krauskopf, A. Senyshyn, C. Dietrich, A. Zevalkink, J. Janek, W. G. Zeier, Influence of Lattice Polarizability on the Ionic Conductivity in the Lithium Superionic Argyrodites Li<sub>6</sub>PS<sub>5</sub>X (X = Cl, Br, I), *J. Am. Chem. Soc.* (2017) **139**, 10909-10918. <https://doi.org/10.1021/jacs.7b06327>
- [39] N. Kaiser, S. Spannenberger, M. Schmitt, M. Cronau, Y. Kato, B. Roling, Ion transport limitations in all-solid-state lithium battery electrodes containing a sulfide-based electrolyte, *J. Power Sources* (2018) **396**, 175-181. <https://doi.org/10.1016/j.jpowsour.2018.05.095>
- [40] F. Walther, R. Koerver, T. Fuchs, S. Ohno, J. Sann, M. Rohnke, W. G. Zeier, J. Janek, Visualization of the Interfacial Decomposition of Composite Cathodes in Argyrodite-Based All-Solid-State Batteries Using Time-of-Flight Secondary-Ion Mass Spectrometry, *Chem. Mater.* (2019) **31**, 3745-3755. <https://doi.org/10.1021/acs.chemmater.9b00770>

## Highlights

- Argyrodite  $\text{Li}_6\text{PS}_5\text{Cl}$  solid electrolyte with 2D morphology was synthesized
- High ionic conductivity was achieved with scalable liquid phase technique
- 2D morphology improves the ionic conduction within the composite electrode
- All solid state lithium ion battery with enhanced rate performance was demonstrated

Journal Pre-proof

**Declaration of interests**

The authors declare that they have no known competing financial interests or personal relationships that could have appeared to influence the work reported in this paper.

The authors declare the following financial interests/personal relationships which may be considered as potential competing interests:

Journal Pre-proof